PAPER

Check for updates

Capacitive behavior of activated carbons obtained from coffee husk†

Nathalia Ramirez,[ab] Fabiana Sardella,[b] Cristina Deiana,[b] Anja Schlosser, [iD][a]
Dennis Müller,[a] Patrick A. Kißling,[a] Lars F. Klepzig[ac] and Nadja C. Bigall [iD] *[ac]

Sustainable agroindustry has presented many challenges related to waste management. Most of its residues are lignocellulosic biomass materials with great application potential due to their chemical composition, hence the use of biomass-derived carbon materials in energy storage has received growing interest in recent years. In this work, highly micro-porous carbonaceous materials using the endocarp of the coffee fruit or coffee husk (CH) as precursor are obtained. Specifically, three different activating agents (KOH, K_2CO_3, and steam) to derive activated carbons (ACs) with good capacitive properties are tested. The properties of ACs such as surface chemistry, texture, crystal graphite size, and order in the carbonaceous structure are assessed and compared. The capacitive behavior inherent to the activation routes is also characterized by means of Cyclic Voltammetry (CV), Galvanostatic Charge/Discharge (GCD) and Electrochemical Impedance Spectroscopy (EIS). The obtained specific capacitance values range from 106 to 138 F g^{-1} for a discharge current of 0.5 A g^{-1}. These results nominate coffee husk as a good precursor of carbonaceous materials suitable for energy storage.

1 Introduction

Due to the imminent depletion of fossil fuels and their negative impact on the environment, the need for developing clean energy has emerged. In this way, the study of new energy storage and/or conversion devices, which help to optimize the use of such renewable resources, has been promoted. Clean and inexhaustible energy sources such as wind and solar, have been limited in their use because of the intermittent generation, which is related to the fluctuating weather conditions. Devices such as batteries and supercapacitors allow store and deliver energy in a regulated way, eliminating the intermittency associated with these sources. Hence, it is of high importance to develop materials for these storage devices using residual biomass from agriculture and agroindustry, which are cheap, abundant and environmentally friendly. It is a challenge for science to provide alternatives for the valorization of these residual materials. In this sense, the use of wastes as precursor for the production of activated carbons, is an important focus of interest. Carbon-based materials as activated carbons (ACs) are

widely used as electrodes, not only because of the aforementioned, but also because of the wide spectrum of electrochemical/physicochemical properties that can be obtained depending on the precursor and the activation route used.[1–3] Among them, the pseudocapacitive effect is one of the most studied properties in porous carbons, since it improves capacitive behavior by means of charge store on the surfaces *via* faradaic processes. In turns, the charge-transfer resistance at the electrode/electrolyte interface can be reduced by this doping effect and, the wettability can be increased for the maximum utilization of the accessible area.[4] Some studies with lignocellulosic biomass show how the presence or incorporation of heteroatoms improves the electrochemical properties (including cycle stability and rate capability) of the derived carbonaceous material.[5–7]

Coffee husk (CH) is a residual material generated in the threshing processes of the coffee industry, which is a lignocellulosic biomass suitable for activated carbon production due to its high fixed carbon content. It is available in high amounts since coffee is widely cultivated in most of the tropic countries. In the period 2016/2017, coffee production in the world reached 152 million 60 kg bags,[8] which generate 2 432 000 ton of coffee husk (CH), according to the relation 16 kg CH/60 kg bag of coffee.[9] This coffee waste has been assessed in some applications, such as: substrates for mushroom cultivation, vermicomposting, and xylanase, among others.[8] On the other hand, CH has also been used as precursor of carbon materials to later be evaluated in adsorption of dyes or contaminants. Different activation paths, both physical (CO_2, steam) and chemical

[a]Institute of Physical Chemistry and Electrochemistry, Leibniz Universität Hannover, Callinstraße 3A, 30167 Hannover, Germany. E-mail: nadja.bigall@pci.uni-hannover. de

[b]Institute of Chemical Engineering, Universidad Nacional de San Juan, Av. Lib. San Martín Oeste 1109, San Juan J5400ARL, Argentina

[c]Cluster of Excellence PhoenixD (Photonics, Optics, and Engineering – Innovation Across Disciplines), Hannover, Germany

† Electronic supplementary information (ESI) available: FTIR spectra, XRD and Raman calculated parameters. See DOI: 10.1039/d0ra06206e

(H$_3$PO$_4$, ZnCl$_2$, KOH, K$_2$CO$_3$), have been developed,[10–12] but only few of these ACs have been measured as electrode material for energy storage applications.[13] Some others lignocellulosic residues have been used as ACs precursors and later successfully evaluated as supercapacitor electrodes, among them are: argan seed shells activated with KOH,[14] peanut shell and rice husks activated with ZnCl$_2$,[15] fallen leaves activated with K$_2$CO$_3$ and KOH,[16] coconut shell activated with steam.[17] A summary of the physicochemical and electrochemical properties of ACs obtained from different biomasses and activation routes has also been provided.[3] According to this analysis, the variations in the electrochemical performance of agricultural waste-based activated carbons depend not only on the surface area of the materials but also on other factors, such as the pore structure and distribution, the electrical conductivity, and surface functionalities.

The development of an AC material by means of a certain route of activation, whether physical or chemical, provides different physicochemical properties such as volume, pore size and shape, crystallinity, functionalities, *etc.* Although each route could generate valuable/different properties, the disadvantages associated with the environment impact, energy consumption, and yield should be also weighed. For example, the activation process using steam as activating agent could be considered an environmentally friendly method. However, its low yield and high energy consumption related to the double thermal process and high activation temperature represent drawbacks.[18] On the other hand, chemical activation methods with alkaline agents exhibits important advantages since they requires lower activation energy, shorter activation times, and they have higher process yields.[19] The present paper analyzes the electrochemical and physicochemical properties of activated carbons developed from coffee husk through different activation routes. In particular, the use of KOH, K$_2$CO$_3$, and steam as activating agents is evaluated. For each synthesized sample, the physicochemical properties, such as pore size distribution (NLDFT), crystalline patterns (XRD), carbon structure orientation (Raman), and surface chemistry (FTIR) are characterized. Furthermore, using a three electrode cell, electrochemical measurements were performed, in particular CV, GCD, and EIS. From these measurements, the capacitive behavior is characterized and a comparative analysis to evaluate how the activation routes impact on the psychochemical and electrochemical properties of the ACs is reported.

2 Results and discussion

2.1 Physicochemical characterization of activated carbons

2.1.1 Textural properties. Textural parameters obtained from N$_2$ adsorption assays are summarized in Table 1. The pore size distributions (PSD) and pore volumes are determined by means of slit/cylindrical NLDFT (non-local density functional theory) equilibrium model. Fig. 1 illustrates the PSD of activated carbons prepared by different activation routes. The influence of the activation route on the porosity of the samples can be clearly observed. While chemical activation with KOH and K$_2$CO$_3$ generates a mainly microporous texture with type I

Table 1 S_{BET} and textural parameters (NLDFT) of ACs from CH obtained by different activation routes

Parameter	CH-steam	CH-KOH	CH-K$_2$CO$_3$
S_{BET} (m^2 g^{-1}) $\pm$ 5%	1447	2275	1156
Total pore volume (cm^3 g^{-1})	0.603	0.890	0.357
Half pore width (Å)	6.36	9.82	7.16
Fitting error NLDFT (%)	0.087	0.026	0.076

adsorption isotherms according to the IUPAC classification, physical activation with steam develops a structure with micro and mesopores, which exhibits a type IV adsorption isotherm with a H3-type hysteresis loop according to the IUPAC classification. The activation with KOH produces a half pore width of 9.8 Å and the highest specific surface area (S_{BET} = 2275 m^2 g^{-1}), which is characteristic of this chemical agent due to its activation route involves the formation of K$_2$CO$_3$ as an intermediate product, which implies a double activation step and consequently higher micropore volumes.[20] Activation with K$_2$CO$_3$ produces a S_{BET} of 1156 m^2 g^{-1} with half pore width around 7.2 Å and the most homogeneous texture, which is typical of this activation route at the applied process temperature, when 800 °C is reached the potassium is at its boiling point and it can diffuse into carbon layers facilitating pores formation, higher temperatures would promote the formation of mesopores by micropores enlarging or combining.[21] On the other hand, the sample activated with steam shows a multimodal distribution with the narrowest micropores width (6.4 Å) and S_{BET} of 1447 m^2 g^{-1}, these results are strongly linked to the features of the coffee husk itself, in other words to its content of ash and volatile matter.[22] A hierarchical porous structure (micro, meso and macropores) is beneficial for offering a large surface area, shortening the ion transport distance, and serving as ion-buffering reservoirs, respectively.[5]

2.1.2 Morphology and microstructure analysis. Scanning electron microscopy (SEM) and high-resolution transmission electron microscopy (HRTEM) images of the samples: CH-
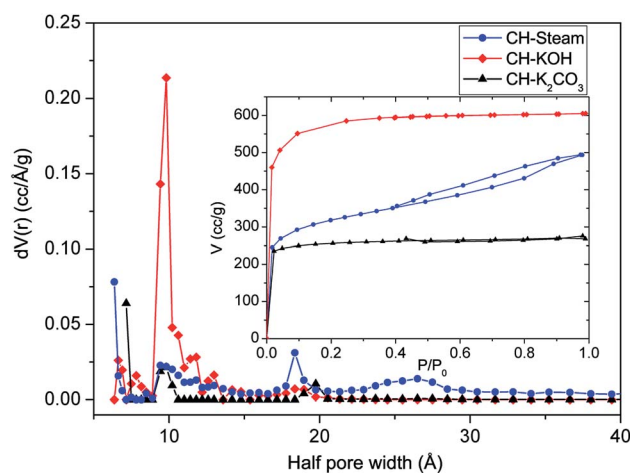

Fig. 1 PSDs and isotherms of AC from CH (activation with steam, KOH, and K$_2$CO$_3$ are in blue, red, and black, respectively). $\pm$5% error.

steam, CH-KOH and CH-K$_2$CO$_3$ are presented in Fig. 2. At the micro-scale level, all the ACs show well developed porous structures with different morphologies related to the applied activation pathway. CH-steam exhibits an irregular and heterogeneous topography, whose external surface has cracks and connected cavities (see Fig. 2a and b). CH-KOH shows slits and collapsed pores (see Fig. 2d and e), which are a result of thermal stress due to the double heat treatment. CH-K$_2$CO$_3$ indicates a uniform and highly macroporous structure with open channels of homogenous sizes between 0.6–1 μm (see Fig. 2g and h). This type of morphology is characteristic of chemical activation with K$_2$CO$_3$.[21,23] In the high-resolution TEM images, the carbon nanocrystal structures of the analysed samples are shown. They present amorphous and turbostratic carbon. The observed differences in the crystal structure of the ACs and the differences in the textural properties are inherently connected. CH-KOH has an amorphous structure with the shortest and disordered graphite nanocrystals (see Fig. 2f). This result matches with the highest values of specific surface area and pore volume of CH-KOH (Table 1). In contrast, the sample CH-K$_2$CO$_3$ with lower S_{BET} shows better growth and ordering of the graphite structure (Fig. 2i). Finally, CH-steam shows an intermediate crystal structure in terms of size with a randomly-oriented graphitic ribbon network structure (see Fig. 2c), which is linked to non-uniform and generally large pores formed at higher synthesis temperatures.[24]

2.1.3 XRD patterns and Raman spectra. In the X-ray diffraction profiles of the analyzed ACs (Fig. 3a), two broad reflections were identified in the following 2θ ranges: 21°–30° and 41°–44°, which correspond to the (002) and (100 & 101) crystal planes, respectively. This effect suggests that the crystallites in the ACs have an intermediate structures between graphite and the amorphous state, known as turbostratic structure or random layer lattice structure.[25] A third reflection could be observed in CH-K$_2$CO$_3$ around 20° which has already been reported in other works and is attributed to saturated carbons by aliphatic chains on the edges of graphene nanoplatelets.[26,27]

The nano-platelet dimensions of the sp^2-ordered crystallites, pseudocrystallite height (L_c) and lateral crystallite dimension
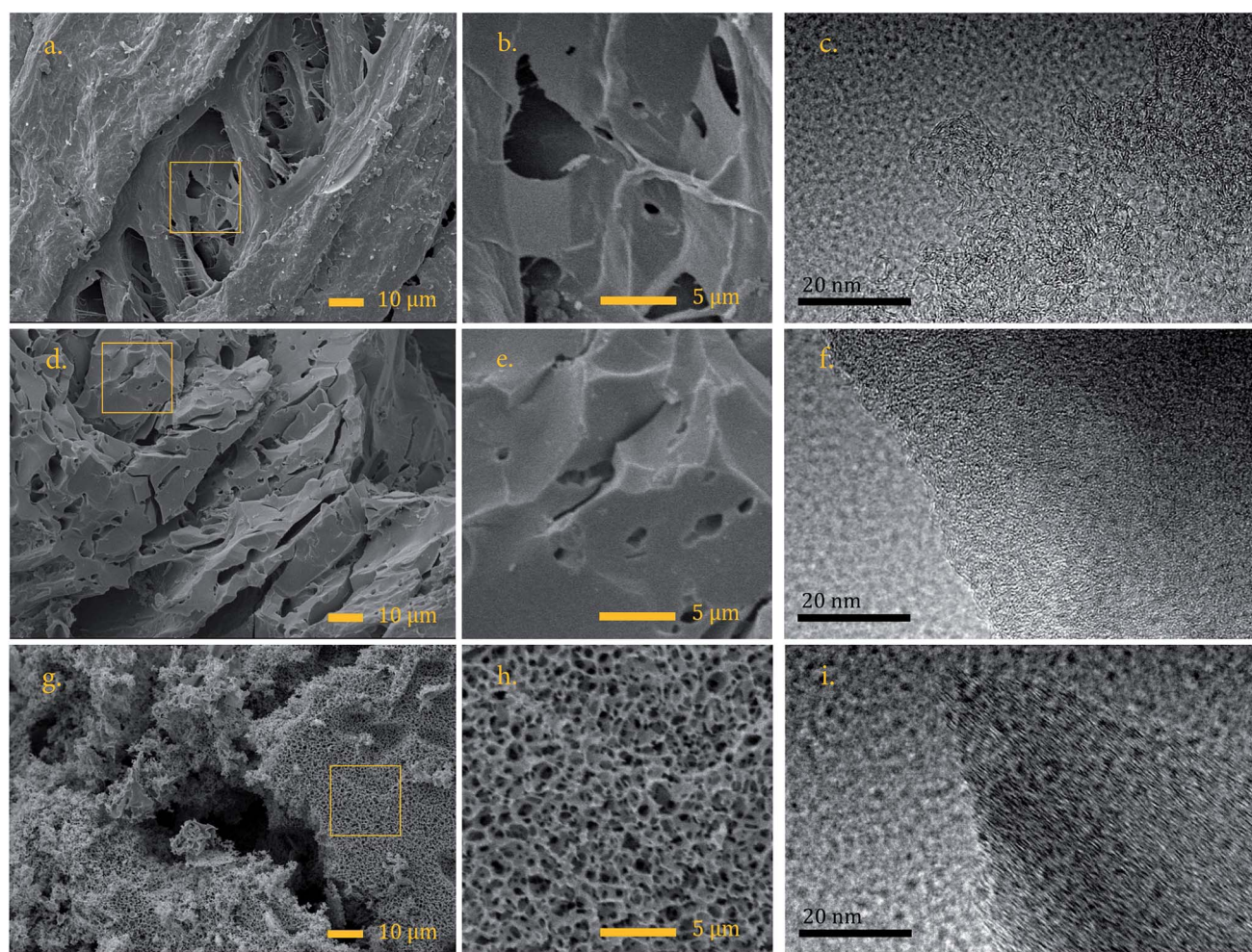

Fig. 2 SEM image of CH-steam (a) and its magnification (b), high-resolution TEM image of CH-steam (c), SEM image of CH-KOH (d) and its magnification (e), high-resolution TEM image of CH-KOH (f), SEM image of CH-K$_2$CO$_3$ (g) and its magnification (h), and high-resolution TEM image of CH-K$_2$CO$_3$ (i).
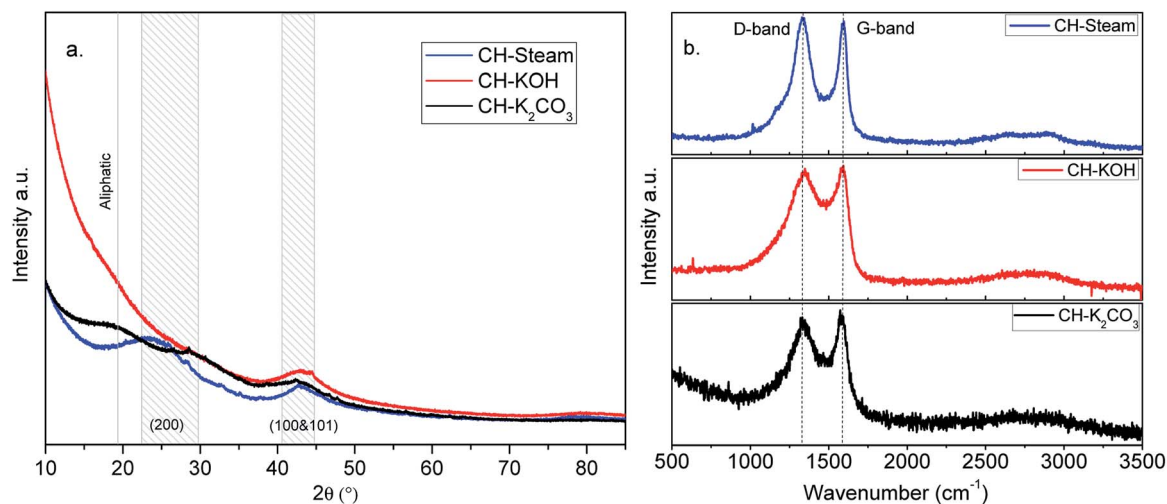
Fig. 3 XRD (a) and Raman (b) spectra of ACs from CH (activation with steam, KOH, and K_2CO_3 are in blue, red, and black, respectively).

(L_a) were calculated for the analyzed samples by applying the Debye–Scherrer equation from the reflection parameters (002) and (100 & 101), respectively.[27] The obtained parameters are shown in Table S1.† All the samples exhibit high background intensity, which indicates that the ACs contain a proportion of highly disordered materials in the form of amorphous carbon. CH-KOH, the sample with the highest specific surface area, shows the greater intensity in the low-angle scatter, which is accordingly related to the sample porosity. Other authors report similar XRD profiles for carbon materials obtained with the same activating agent.[16,28]

The wider the reflection is and greater the shift to lower angle, the greater the degree of disorder,[29] (see FWHM in the Table S1†). The reflection of the (002) plane in the sample CH-KOH is very weak, broad and it is displaced towards lower angles, which indicates more space between layers. The reflections of (100 & 101) planes are clearly observed and appear nearly in the same angle in all the spectra. The crystalline parameters of the analyzed samples differ widely according to the activating agent. The activation with KOH generates a basic structural unit of graphite with the smallest dimensions L_a and L_c, as well as, the biggest interplanar distance d_{002}. On the other hand, the activation with K_2CO_3 produces the most ordered crystalline structure with the biggest crystallite dimensions and lowest interplanar distance, which is in agreement with the TEM images previously analyzed.

In Fig. 3b, Raman spectra of the analyzed samples are shown. The so-called graphite (G band) around 1582 cm^{-1} and the so-called disorder-induced (D band) around 1350 cm^{-1} can be identified in the spectra of the ACs. The D band is assigned to the breathing mode of k-point phonons of A_{1g} symmetry for the disordered graphite and the G band is assigned to the E_{2g} mode of 2D graphite.[30] As observed, the full width at half maximum (FWHM) of the G band ranges from 66 to 95 cm^{-1} (Table S2†). This value is higher than one reported for highly oriented pyrolytic graphite (15–23 cm^{-1}), which indicates a low degree of crystalline order in the studied samples. The parameters

obtained by means of the deconvolution of the characteristic bands in the spectra using Lorenz fits are summarized in Table S2.† In the Raman spectrum of graphite, there exists a correlation between the ratio of intensities ($R = I_D/I_G$) and the reciprocal of the crystallite size parameter ($1/L_a$).[31] This correlation is also observed in the analyzed samples (see parameter in Tables S1 and S2†). For carbon samples, the higher R is, the greater the degree of disorder. This demonstrates that the sample with the most disordered graphite structure is CH-KOH and the least disordered is CH-K_2CO_3.

In other words, some of the obtained parameters from the XRD patterns and Raman spectrum of a carbon sample are used as indicators of its graphitization degree. Lower d_{002} and R values, as well as, higher L_a values suggest greater graphitization.[31] In turn, the graphitization degree is an indicator of the electrical conductivity, the higher the graphitization the greater the conductivity.[32,33] In this way, improving the graphitization of an AC simultaneously enhances the electric conductivity of the electrode and its surface wettability towards aqueous electrolytes, which can facilitate ion diffusion and electron transport, thus improving the electrochemical performance.[1,34] This means that the crystalline properties of CH-K_2CO_3 could promote a better capacitive behavior regarding CH-KOH.

2.1.4 FTIR spectrum analysis. The FTIR spectra of CH and the activated carbons obtained by different routes are presented in Fig. S1.† The broad band around 3400–3300 cm^{-1} is attributed to the stretching vibrations of O–H bonds in water molecules, and also to O–H groups present in cellulose, hemicellulose, and lignin.[35] The band at 2925 and 2854 cm^{-1}, which is present in the spectrum of the precursor, is due to the C–H stretching vibrations in methylene groups and it is characteristic of lignocellulosic materials.[30,36]

The band at 2649 cm^{-1} in CH-K_2CO_3 and CH-KOH might be ascribed to the traces of potassium carbonates, this indicates that in spite of the washing, a trace amount of potassium remained chemically bounded inside the pore structure.[37] The bands in the range 2200–1945 cm^{-1}, which appear in the

spectra of all tested ACs samples, are ascribed to N–H⋯O stretching and bending intramolecular hydrogen bonding,[38] these signals could be originating from the content of proteins and caffeine in the precursor, 9.2 and 1.2 wt% respectively.[8] According to the bibliography,[37] it could be assumed that the samples have surface functionalities with C=O (carboxylic, anhydride, lactone, and ketene groups having IR bands at 1750–1630 cm^{-1}), C=C (1640–1430 cm^{-1}), and C–O (lactonic, ether, phenol, *etc.*, with a intensive band at 1300–1000 cm^{-1}). These bands, present in precursor samples, are some times found in ACs, indicating that these groups were not completely removed by activation. The band at 1475 to 1350 cm^{-1}, appears in precursor spectrum and it is related to C–H deformation vibrations in lignin and carbohydrates.[39]

Comparing AC samples with the precursor, a change in the functionalization is observed since bands appear in other wavelengths, additionally an increase in their surface functionalization is observed, especially in the sample activated with K_2CO_3. It is worth to mention that surface functional groups produce a pseudocapacitive effect, which improves capacitive behavior by means of charge store on the surfaces *via* faradaic processes. In turns, the charge-transfer resistance at the electrode/electrolyte interface is reduced by this doping effect and, the wettability is increased for the maximum utilization of the accessible area.[4]

2.2 Electrochemical characterization of activated carbons

2.2.1 Cyclic voltammetry (CV). In order to characterize the electrochemical properties of the CH-steam, CH-KOH, CH-K_2CO_3 cells, cyclic voltammetry is performed. The obtained curves are shown in Fig. 4. All the AC cells present typical rectangular CV curves, being more rectangular at lower scan rates. This is due to the fact, that higher scan rates normally generate large ohmic resistance which causes distortion in the CV loop resulting in a narrower loop with an oblique angle.[3] At low scan rate, all the AC cells exhibit similar voltammogram areas, however, at higher scan rates the CVs shape and areas differ widely.

The CH-K_2CO_3 cell has the largest CV area and presents better rectangular shape than CH-steam and CH-KOH at 10 mV

s^{-1}, which indicates higher capacitance and a better rate capability. On the one hand, this effect is due to the surface chemistry of CH-K_2CO_3 with presence of heteroatoms, which improves the wettability of the carbon and induce pseudocapacitive behavior, enhancing the electron conductivity and the specific capacitance from the surface faradaic reactions with electrolyte ions, respectively.[6] These functionalities have more influence on the electrochemical behavior than other physico-chemical properties,[3] which corresponds to the obtained results for CH-K_2CO_3. Despite its lower specific surface area, it shows the best capacitive behavior. On the other hand, the crystalline properties previously analysed by TEM, XRD and Raman (size of the graphene sheets and orientation of the crystallites), suggest that CH-K_2CO_3 is the sample with the highest electric conductivity.[32] This characteristic explains why the cell CH-K_2CO_3 exhibits better rectangular CV curve. Additionally, the CH-K_2CO_3 SEM image reveals the existence of channels (see Fig. 2g and h), which supply pathways that promote a fast ion transport and serving as ion-buffering reservoirs,[5] which are favourable for accelerating the kinetic process of ion diffusion in the electrodes enhancing the power density and rate capability.[40] This also applies for the cell CH-steam, which according to the N_2 adsorption analysis corresponds to a mesoporous carbon that has demonstrated an intermediate capacitive behaviour due to this fact, as well as, its crystal properties.

In Fig. S2,† the specific capacitance (C_s) of all AC cells is plotted as a function of the scan rate in order to determine the rate capability. The value of the specific capacitance tends to be higher at lower scan rate, since a more homogeneous electric potential is created along the material with minimal variations of potential and dispersion of capacitance in the porous electrode.[13] As it can be seen in the plot, C_s of all the AC cells depends on the scan rate, however, CH-KOH is more strongly dependent. The obtained rate capability for the cells CH-steam, CH-KOH and CH-K_2CO_3 are 19, 11 and 39%, respectively, which are calculated using the CV measurements at 1 and 10 mV s^{-1}. The low rate capability of the CH-KOH sample is directly related to a low electrical conductivity associated to its reduced graphitization degree and poor surface chemistry (see TEM, XRD, and FTIR results in Sections 2.1.2, 2.1.3 and 2.1.4), as well
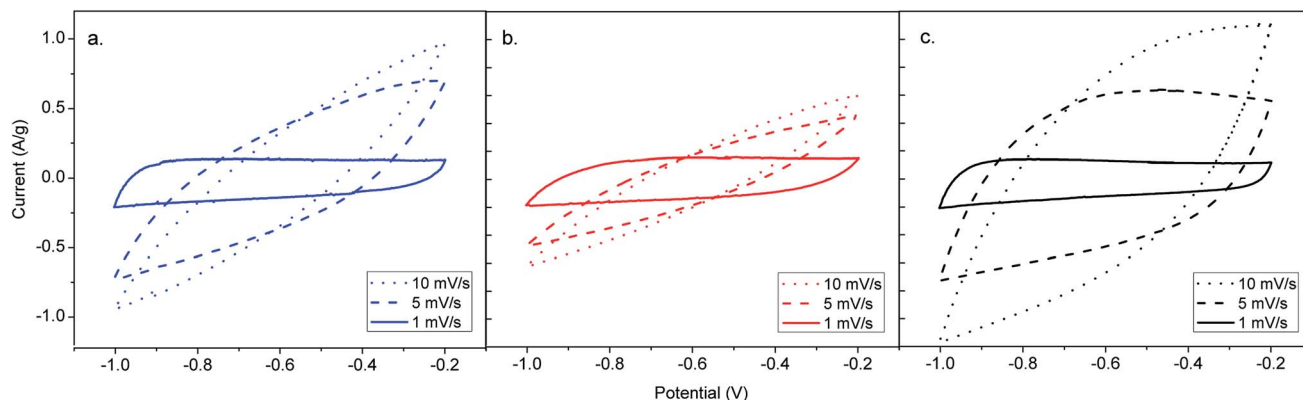

Fig. 4 CV curves of ACs from CH obtained by different activation routes. (a) CH-steam, (b) CH-KOH, (c) CH-K_2CO_3.

as, to a limited ion mobility caused by its high microporosity (see N_2 adsorption results in Section 2.1.1). These factors hinder a fast accessibility of ions into the whole carbon matrix and therefore the capacitive properties are reduced.[5,32,40,41]

Fig. 5 shows how the specific capacitance of the activated carbon electrodes evolves with the number of cycles. The cyclic stability at 1000 cycles obtained for the cells CH-steam, CH-KOH and CH-K_2CO_3 are 98, 99 and 97%, respectively. These values agree with stability typical of EDLC from agricultural waste biomass.[3] It is worth to mention that the negative trend of the stability curve of the CH-K_2CO_3 cell (slightly bigger than the other samples) is related to the faradaic processes that take place on the surface. In addition, the increase of capacitance during the first cycles is linked to the improvement in the wettability conferred by the presence of heteroatoms.[5]

2.2.2 Galvanostatic charge/discharge (GCD). Fig. 6 shows the GCD curves at a current density of 0.5 A g^{-1} for the evaluated carbonaceous materials. As it can see in this figure, all the AC cells show triangular GCD curves characteristic for this type of materials. CH-K_2CO_3 and CH-steam exhibit longer charge and discharge time than CH-KOH which means that they have higher capacitance. In all the AC cells sharp voltage drops at the beginning of the discharge are observed, which are the results of diffusion-limited mobility of the electrolyte ions in the electrode pores.[42] Those voltage drops can also be associated with several aspects such as:[32,43]

• The absence of a conductive additive

• The use of a polymeric binder in the electrodes construction

• The resistance at the interface between the current collector and the active layer

• The low conductivity of highly porous activated carbon (the larger the total pore volume of the AC sample is, the lower its intrinsic electrical conductivity is).

In particular, CH-KOH has the most pronounced voltage drop and the highest distortion in the CV curve. This effect is
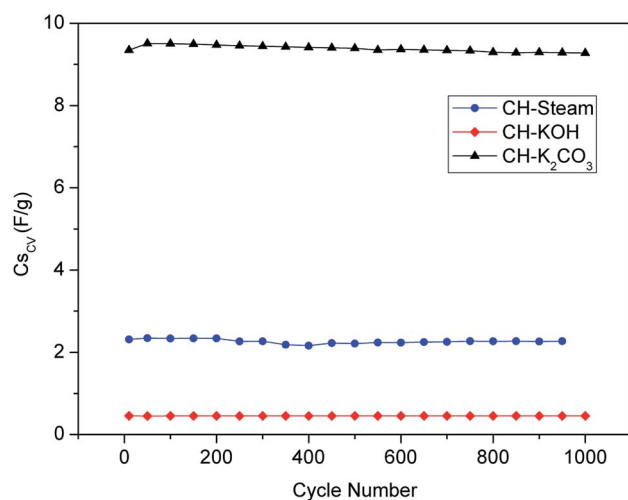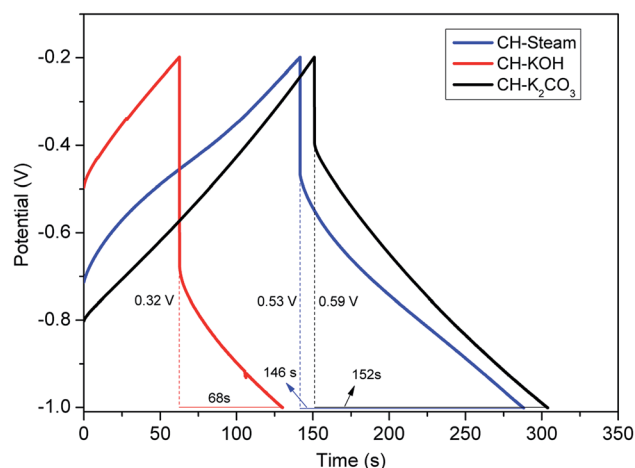

Fig. 6 GCD curves of AC cells from CH (activation with steam, KOH, and K_2CO_3 are in blue, red, and black, respectively).

due to its disordered structure and low graphitization degree, which imply a lower electrical conductivity. As mentioned, these characteristics produce a negative effect in the electrolyte penetrability into the electrode active layer and, consequently, in the ion diffusion into the micropores. In contrast, CH-K_2CO_3 shows the smallest voltage drop and a better rectangular CV shape that agree with the obtained physicochemical properties as described in the previous sections.

The observations made from GCD curves agree with the conclusion drawn from the CV. Table 2 summarizes the parameters obtained from GCD: Δt (discharge time, s), ΔV (potential window subtracting iR drop, V), iR drop (voltage drop, V), C_s (specific capacitance, F g^{-1}), ESR (equivalent series resistance, ohms), E (energy density, W h kg^{-1}), and P (power density, W kg^{-1}). The existence of internal resistance reduced the device energy and power performance.

2.2.3 Electrochemical impedance spectroscopy (EIS). The frequency response of the studied AC cells was characterized by means of electrochemical impedance spectroscopy (EIS). Fig. 7a shows the Nyquist plots obtained from the EIS experimental data. The measurements are done in the frequency range from 100 kHz to 10 mHz under open circuit with a perturbation of 5 mV. The Nyquist diagrams obtained exhibit the typical curve of an electric double-layer capacitor (EDLC), which consist of a semicircle in the high frequency region, followed by a straight

Fig. 5 Cyclic stability from CV at 100 mV s^{-1} of ACs from CH (activation with steam, KOH, and K_2CO_3 are in blue, red, and black, respectively).

Table 2 GCD parameters of AC cells from CH obtained by different activation routes

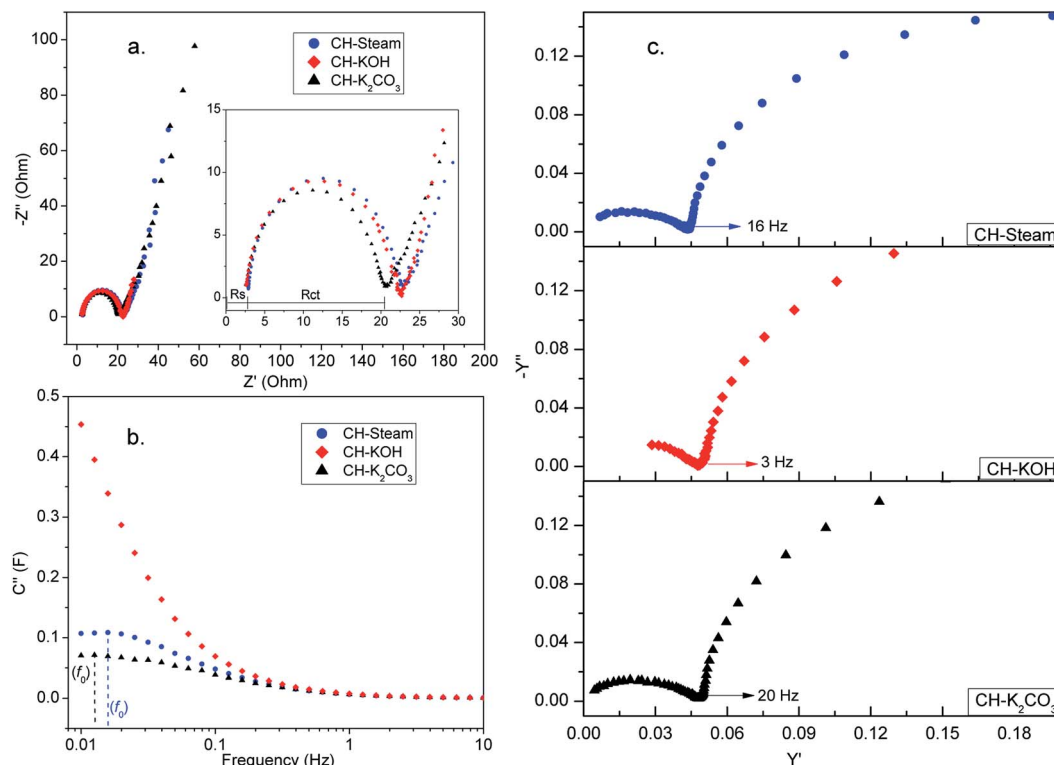| Parameter	Units	CH-steam	CH-KOH	CH-K_2CO_3
Δt	s	146	68	152
ΔV	V	0.53	0.32	0.59
iR drop	V	0.27	0.48	0.21
C_s	F g^{-1}	138	106	129
ESR	ohms	0.27	0.26	0.21
E	W h kg^{-1}	5.40	1.51	6.29
P	W kg^{-1}	133.25	80	149.19

Fig. 7 Nyquist plot (a), imaginary part of the complex capacitance (b), and admittance (c) of AC cells from CH (activation with steam, KOH, and K_2CO_3 are in blue, red, and black, respectively).

line segment with a slope near 45° in the intermediate frequency region and another straight line with steeper slope in the low frequency region.

From Nyquist plot, two resistances (R_s and R_{ct}) are obtained directly. R_s comes from the bulk solution resistance, its magnitude depends on the electrolyte conductivity. R_{ct} depends on the conductivity of the carbon particles and the contact between them, the contact between the active layer and the current collector, and the electrolyte ionic resistance inside the pores of the electrode.[43] For the analyzed AC cells R_s has a similar value, while R_{ct} differs, especially for the CH-K_2CO_3 cell which shows the smallest value. This result is due to the crystal properties of CH-K_2CO_3 which suggest that this sample has better conductivity than the other ones. On the other hand, the noticeable semicircles in the Nyquist plot in all the samples

could be associated to contact resistances between the carbon layer and the current collector.

Other two important parameters could be also analyzed from the EIS data, the relaxation time ($\tau_0 = 1/f_0$) and the knee frequency (f_k). The first one can be calculated from a characteristic frequency f_0, corresponding to the maximum in the imaginary capacitance plot (Fig. 7b). At f_0, half of the low-frequency capacitance is reached, higher power delivery corresponds to lower τ_0 values. The second one corresponds to the transition point between the two semi-circles in the admittance plot (Fig. 7c), f_k is the indication of the power capability of the cell.

Table S3† summarizes the parameters obtained from EIS data for the analyzed samples. The τ_0 value for CH-KOH cell cannot be calculated because the maximum in the C'' curve is below the range of measured frequencies. The CH-steam cell

Table 3 Processing conditions of activated carbons from coffee husk[12]

| Sample | Carbonization | | Activation | | | | | |
	T (°C)	Time (min)	Activation agent	IR^a (w AA (g)/ w P (g))	Q_{steam} (mL min^{-1})	Time (min)	T (°C)	Yield (%)
CH-steam	500	120	Water steam	n/a	0.85	105	910	7.28
CH-KOH	500	120	Potassium hydroxide	2	n/a	60	800	15.15
CH-K_2CO_3	n/a	n/a	Potassium carbonate	2	n/a	60	800	18.9

^{a} IR is the impregnation ratio of activating agent (AA) and precursor (P). For activation with KOH, P is carbonized-CH while, in the activation with K_2CO_3, P is CH.

shows the smallest τ_0 compared to the other AC cells which indicates a faster charge storage/delivery. The sample activated with steam is the only one that contains mesopores, this enables a soft diffusion of ions, which implies a lower relaxation time. τ_0 values are within the same order of magnitude as those reported beforehand for electrodes derived from carbon nanotube and biomass carbon.[42] On the other hand the knee frequency values show that CH-K_2CO_3 cell have the best rate capability.

Table S4† shows the specific capacitance values reported by other authors for electrodes made from biomass carbon, which were obtained by means of using the activating agents studied in this work. All data was taken from GCD measurements. The values obtained for the coffee husk in this work are above those previously reported for this sort of biomass. In relation to other precursors, which have different characteristics and compositions, the obtained values were in the same order.

3 Conclusions

Activated carbons developed from coffee husk through different activation routes were tested. The influence of the activating agent (KOH, K_2CO_3, or steam) over the electrochemical behavior was evaluated. The ACs exhibited high specific surface areas (over 1100 $m^2\ g^{-1}$) and variations in their pore size distribution, crystallinity, and functionalization. From the obtained results by means of different electrochemical characterization techniques, it can be concluded that in terms of capacitance and power capability CH-K_2CO_3 and CH-steam have better performance compared to CH-KOH, despite of both having large differences in their physicochemical properties. The good capacitive behavior of CH-steam was related to the presence of mesopores in the structure. This, facilitates a soft diffusion of ions and confers it a lower relaxation time. For CH-K_2CO_3, by contrast, was associated with its greater functionalization and crystallinity. In this way, ion diffusion in the micropores is enabled due to better conductivity in the carbon matrix. Additionally, it should also be highlighted that the sample activated with K_2CO_3, besides having a good capacitive behavior, is obtained by an environmentally friendly activation route, with the lowest energy consumption and the highest yield. This work shows that, coffee husks is a lignocellulosic waste suitable to obtain highly porous materials with good capacitive behavior. This constitutes a contribution to the sustainability of agroindustry since, through this, an opportunity for CH final disposal is generated and additionally, the high potential of this biomass is advantaged. On the other hand, a contribution in the state of the art of sustainable materials for the building of energy storage devices is provided.

4 Experimental section

4.1 Precursor and activated carbon preparation

Coffee husk (CH) is used as precursor, which is dried in an oven at 70 °C for 24 h before the activation procedures. Activated carbons (ACs) by using physical activation with steam and chemical activation with KOH and K_2CO_3 are developed. The activation procedures are performed according to the methods described in a previous study.[12] Table 3 summarizes the processing conditions to obtain the studied ACs. ACs are denoted as CH-X, where CH is coffee husk and X is related to the activating agent (steam, KOH, and K_2CO_3).

4.1.1 Activation with steam. To perform the physical activation, the precursor is carbonized in a stainless steel reactor with a heating rate of 4 °C min^{-1} until reach 500 °C, this temperature is kept during 120 min in absence of oxygen. Afterwards, the carbonized precursor is subjected to a thermal process in a 30 mm diameter stainless steel reactor with a heating rate of 5 °C min^{-1} until reach 910 °C, this temperature is kept during 105 min while injecting super heated steam at 0.85 mL min^{-1}. Heating and cooling are carried out under inert atmosphere. This sample is identified as CH-steam.

4.1.2 Activation with KOH. CH is carbonized at the same conditions described in 4.1.1. Later, this is wetted with KOH solution at 80% w/w in an impregnation ratio of 2 g KOH/g carbonized-CH, and then dried in a stove at 130 °C for 24 h. The impregnated and dried sample is transferred to a stainless steel cylindrical reactor for its thermal treatment in absence of oxygen with a heating rate of 10 °C min^{-1} until reach 800 °C, this temperature is kept for 60 min. The product is cooled to room temperature and then washed with 0.5 L of 0.1 M HCl solution and distilled water until reaching a pH between 6 and 7. This sample is identified as CH-KOH.

4.1.3 Activation with K_2CO_3. CH is mixed with a saturated solution of K_2CO_3 in an impregnation ratio of 2 g K_2CO_3/g CH and taken to a stove at 130 °C overnight. Then the impregnated and dried sample is placed in a stainless steel cylindrical reactor and activated at 800 °C for 60 min. To remove residual K_2CO_3, the sample is washed with 0.5 L of 0.1 M HCl solution and distilled water until reaching a pH between 6 and 7. This sample is named CH-K_2CO_3.

4.2 Preparation of coated electrodes

To prepare the electrodes, conductive indium tin oxide coated glass slides (ITO glass) are used as substrates. ACs are immobilized on them by dropcasting a slurry of respective AC (CH-steam, CH-KOH, and CH-K_2CO_3) and polyvinylidene fluoride in dimethyl sulfoxide (PVDF/DMSO) and drying it overnight at 80 °C and 20 mbar in a vacuum oven. The slurry is prepared by crushing AC in a mortar and then mixing it with PVDF/DMSO, the ratio of AC and PVDF in the slurry is 1 : 0.05.

4.3 Physicochemical characterization

Nitrogen sorption measurements are carried out with a Quantachrome Nova 3200e, prior to the measurement the AC samples were degassed under vacuum for 24 h at 200 °C. Based on the collected data, the pore size distribution is determined using the Density Functional Theory (DFT). Specifically, the equilibrium of the isotherm is fitted using the Non Local Density Functional Theory (NLDFT, slit/cylindrical pores). The isotherms are analyzed with the software Quantachrome NovaWin.

The morphology and nanostructure of the ACs was studied by scanning electron microscopy (SEM) using a (Zeiss Supra 35 VP), and high-resolution transmission electron microscopy (HRTEM) with a FEI Tecnai G2 F20 TMP (operated at 200 kV), respectively.

X-ray diffraction patterns of the samples are obtained by means of Bruker AXS/D8 Advance diffractometer, between $2\theta = 5°$ and $85°$ using KαCu radiation ($\lambda = 0.15418$ nm, 40 kV, 30 mA) at a scan rate of $2\theta = 4°$ min^{-1}. Raman spectroscopy is used to measure the degree of orientation of the graphitic structure in the ACs. The spectra are measured with a Bruker Senterra Raman microscope using a laser wavelength of 532 nm and a laser power of 5–10 mW.

ATR-FTIR spectra of CH and CH-ACs are recorded to characterize the surface chemistry. Powder samples are analyzed at room temperature using a Agilent Cary 630 FTIR spectrometer equipped with a diamond attenuated total reflectance (ATR) sampling accessory between 4000 and 630 cm^{-1} at a resolution of 2 cm^{-1}.

4.4 Electrochemical characterization

The assessment of the capacitive behavior of the ACs from CH are carried out in a self-built three electrode cell, with KOH (6 M) as electrolyte. A platinum wire, a Ag/AgCl electrode (3 M NaCl, purchased from BASi), and the AC coated electrode are used as counter, reference, and working electrode, respectively. Cyclic voltammetry (CV) and galvanostatic charge/discharge (GCD) are performed with a Potentiostat/Galvanostat Metrohm Autolab PGSTA T204, while electrochemical impedance spectroscopy (EIS) is done with a Modulab XM ECS potentiostat from Solatron. CV curves are measured in a potential window between -1 and -0.2 V (*versus* Ag/AgCl) with a scan rate of 1, 5, or 10 mV s^{-1}. The specific capacitance obtained from CV ($C_{s_{cv}}$, F g^{-1}) is calculated from the area (mathematical area, integration tool Origin) under the CV curve (A_{cv}, A V g^{-1}), the scan rate (s, V s^{-1}), and the voltage window (V, V) as follows,

$$C_{s_{cv}} = \frac{A_{cv}}{s\,V}.$$

For GCD measurements, a discharge current of 0.5 A g^{-1} is applied. The specific capacitances (C_s, F g^{-1}) and the equivalent series resistances (ESR, ohms) for the analyzed samples are calculated from GCD data as follows,

$$C_s = \frac{I\Delta t}{m\Delta V}, \quad \text{ESR} = \frac{iR_{drop}}{2I},$$

where I (A), Δt (s), m (g), ΔV (V) and iR_{drop} (V), are: the discharge current, the discharge time, the mass of the electroactive materials in the electrodes, the potential window, and the voltage drop respectively. Furthermore, the energy density (E, W h kg^{-1}) and power density (P, W kg^{-1}) of the characterized AC cells are calculated from the GCD data as shown below,

$$E = \frac{1}{2}C_s(\Delta V)^2, \quad P = \frac{E}{\Delta t}.$$

EIS tests are performed by applying an amplitude of 5 mV in the frequency range from 0.1 Hz to 100 kHz. To perform the analysis of EIS results, admittance data are calculated as follows,

$$A = \frac{1}{Z}, \quad A = \frac{Z'}{\|Z\|^2} - j\frac{Z''}{\|Z\|^2},$$

where Z' is the real impedance, Z'' is the imaginary impedance and $\|Z\|$ is the impedance module. In addition, the corresponding real and imaginary admittances are calculated as $Z'/\|Z\|^2 = Y'$ and $-Z''/\|Z\|^2 = Y''$. The imaginary capacitance from the complex capacitance is also determined as follows,

$$C = \frac{1}{j\omega(Z' + jZ'')},$$

$$C' = -\frac{Z''}{\omega\|Z\|^2}, \quad C'' = \frac{Z'}{\omega\|Z\|^2},$$

where $\omega = 2\pi f$ is the angular frequency, C is the complex capacitance and C' and C'' are real and imaginary parts of the complex capacitance, respectively.

Conflicts of interest

The authors declare no conflict of interest.

Acknowledgements

Notes and references

1 H. Lu and X. Zhao, *Sustainable Energy Fuels*, 2017, **1**, 1265–1281.
2 J. Wang, P. Nie, B. Ding, S. Dong, X. Hao, H. Dou and X. Zhang, *J. Mater. Chem. A*, 2017, **5**, 2411–2428.

3 A. M. Abioye and F. N. Ani, *Renewable Sustainable Energy Rev.*, 2015, **52**, 1282–1293.

4 S. K. Park, S. H. Kwon, S. G. Lee, M. S. Choi, D. H. Suh, P. Nakhanivej, H. Lee and H. S. Park, *ACS Energy Lett.*, 2018, **3**, 724–732.

5 H. Zhang, M. Lu, H. Wang, Y. Lyu, D. Li, S. Sun, J. Shi and W. Liu, *Sustainable Energy Fuels*, 2018, **2**, 2314–2324.

6 D. Chen, L. Yang, J. Li and Q. Wu, *ChemistrySelect*, 2019, **4**, 1586–1595.

7 S. K. Park, H. Lee, M. S. Choi, D. H. Suh, P. Nakhanivej and H. S. Park, *Energy Storage Materials*, 2018, **12**, 331–340.

8 B. Janissen and T. Huynh, *Resour., Conserv. Recycl.*, 2018, **128**, 110–117.

9 J. Montilla Pérez, J. Arcila Pulgarín, M. Aristizábal Loaiza, E. C. Montoya Restrepo, C. Oliveros Tascón, G. Puerta Quintero and G. Cadena Gómez, *Av. Tec. Cenicafe*, 2008, **370**, 1–8.

10 M. Baquero, L. Giraldo, J. Moreno, F. Suárez-García, A. Martínez-Alonso and J. Tascon, *J. Anal. Appl. Pyrolysis*, 2003, **70**, 779–784.

11 S. S. Brum, M. L. Bianchi, V. L. d. Silva, M. Goncalves, M. C. Guerreiro and L. C. A. d. Oliveira, *Quim. Nova*, 2008, **31**, 1048–1052.

12 A. Mamaní, N. Ramírez, C. Deiana, M. Giménez and F. Sardella, *J. Environ. Chem. Eng.*, 2019, 103148.

13 J. V. Nabais, J. G. Teixeira and I. Almeida, *Bioresour. Technol.*, 2011, **102**, 2781–2787.

14 A. Elmouwahidi, Z. Zapata-Benabithe, F. Carrasco-Marín and C. Moreno-Castilla, *Bioresour. Technol.*, 2012, **111**, 185–190.

15 X. He, P. Ling, J. Qiu, M. Yu, X. Zhang, C. Yu and M. Zheng, *J. Power Sources*, 2013, **240**, 109–113.

16 Y.-T. Li, Y.-T. Pi, L.-M. Lu, S.-H. Xu and T.-Z. Ren, *J. Power Sources*, 2015, **299**, 519–528.

17 J. Mi, X.-R. Wang, R.-J. Fan, W.-H. Qu and W.-C. Li, *Energy Fuels*, 2012, **26**, 5321–5329.

18 X.-f. Tan, S.-b. Liu, Y.-g. Liu, Y.-l. Gu, G.-m. Zeng, X.-j. Hu, X. Wang, S.-h. Liu and L.-h. Jiang, *Bioresour. Technol.*, 2017, **227**, 359–372.

19 A. El-Hamouz, H. S. Hilal, N. Nassar and Z. Mardawi, *J. Environ. Manage.*, 2007, **84**, 83–92.

20 J. Wang and S. Kaskel, *J. Mater. Chem.*, 2012, **22**, 23710–23725.

21 I. I. Gurten, M. Ozmak, E. Yagmur and Z. Aktas, *Biomass Bioenergy*, 2012, **37**, 73–81.

22 A. Aworn, P. Thiravetyan and W. Nakbanpote, *J. Anal. Appl. Pyrolysis*, 2008, **82**, 279–285.

23 I. Okman, S. Karagöz, T. Tay and M. Erdem, *Appl. Surf. Sci.*, 2014, **293**, 138–142.

24 G. Yushin, A. Nikitin and Y. Gogotsi, *Carbon Nanomater.*, 2006, 211–254.

25 A. C. Lua and T. Yang, *J. Colloid Interface Sci.*, 2004, **274**, 594–601.

26 C. Sisu, R. Iordanescu, V. Stanciu, I. Stefanescu, A. Vlaicu and V. Grecu, *Dig. J. Nanomater. Bios.*, 2016, **11**, 435–442.

27 O. O. Sonibare, T. Haeger and S. F. Foley, *Energy*, 2010, **35**, 5347–5353.

28 B. S. Girgis, Y. M. Temerk, M. M. Gadelrab and I. D. Abdullah, *Carbon Lett.*, 2007, **8**, 95–100.

29 J. Baek, H.-M. Lee, J.-S. Roh, H.-S. Lee, H. S. Kang and B.-J. Kim, *Microporous Mesoporous Mater.*, 2016, **219**, 258–264.

30 K. Wang, N. Zhao, S. Lei, R. Yan, X. Tian, J. Wang, Y. Song, D. Xu, Q. Guo and L. Liu, *Electrochim. Acta*, 2015, **166**, 1–11.

31 A. Cuesta, P. Dhamelincourt, J. Laureyns, A. Martinez-Alonso and J. M. Tascon, *J. Mater. Chem.*, 1998, **8**, 2875–2879.

32 A. Barroso Bogeat, *Crit. Rev. Solid State Mater. Sci.*, 2019, 1–37.

33 L. Sun, C. Tian, M. Li, X. Meng, L. Wang, R. Wang, J. Yin and H. Fu, *J. Mater. Chem. A*, 2013, **1**, 6462–6470.

34 Z. Yu, L. Tetard, L. Zhai and J. Thomas, *Energy Environ. Sci.*, 2015, **8**, 702–730.

35 L. Muniandy, F. Adam, A. R. Mohamed and E.-P. Ng, *Microporous Mesoporous Mater.*, 2014, **197**, 316–323.

36 Y. Huang, E. Ma and G. Zhao, *Ind. Crops Prod.*, 2015, **69**, 447–455.

37 H. Deng, G. Li, H. Yang, J. Tang and J. Tang, *Chem. Eng. J.*, 2010, **163**, 373–381.

38 A.-N. A. El-Hendawy, *J. Anal. Appl. Pyrolysis*, 2006, **75**, 159–166.

39 L. Luo, C. Xu, Z. Chen and S. Zhang, *Bioresour. Technol.*, 2015, **192**, 83–89.

40 X. Wei, X. Jiang, J. Wei and S. Gao, *Chem. Mater.*, 2016, **28**, 445–458.

41 W. G. Pell and B. E. Conway, *J. Electroanal. Chem.*, 2001, **500**, 121–133.

42 R. Farma, M. Deraman, I. Talib, R. Omar, J. Manjunatha, M. Ishak, N. Basri and B. N. Dolah, *Int. J. Electrochem. Sci.*, 2013, **8**, 257–273.

43 C. Lei, F. Markoulidis, Z. Ashitaka and C. Lekakou, *Electrochim. Acta*, 2013, **92**, 183–187.